Journal of Colloid and Interface Science 683 (2025) 139–149

Contents lists available at ScienceDirect

Journal of Colloid And Interface Science

journal homepage: www.elsevier.com/locate/jcis

Regular Article

Morphological dynamics of thin liquid films formed by bubbles oscillating near a free surface: Experimental and numerical investigation

Lorenzo Lombardi *, Pasquale Calabrese, Daniele Tammaro, Pier Luca Maffettone

Department of Chemical, Materials and Production Engineering, University of Naples Federico II, Italy

GRAPHICAL ABSTRACT

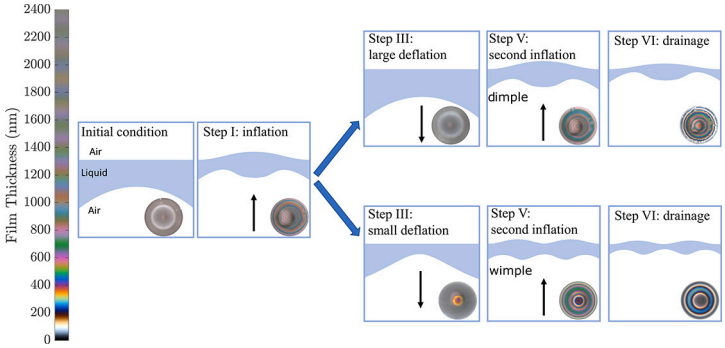

ARTICLE INFO

MSC:
0000
1111

Keywords:
Thin liquid film
Drainage
Interfacial viscoelasticity
Interferometry
Wimple
Dimple
Bovine serum albumin
BSA
Sodium dodecylsulfate
SDS

ABSTRACT

Hypothesis: Bubbles oscillating near a free surface are common across numerous systems. Thin liquid films (TLFs) formed between an oscillating bubble and a free surface can exhibit distinct morphological features influenced by interfacial properties, evaporation, and deformation history. We hypothesize that a continuous film presence throughout oscillation results in a wimple morphology, whereas intermittent film presence leads to a dimple formation. Additionally, we propose that the thickness of a wimpled film depends solely on the capillary number Ca, whether the bubble oscillates toward and away from the free surface or is pressed against it in two consecutive motions.

Experiments: Using dynamic film interferometry, we investigate the morphology and drainage of TLFs formed with BSA and SDS surfactants. Controlled bubble oscillations allow us to test various deformation histories, and a lubrication theory-based model aids in interpreting the experimental findings.

Findings: Experiments confirm that film morphology is heavily influenced by deformation history, with continuous film presence throughout the entire deformation process leading to wimple formation. A modified lubrication-theory-based scaling captures the universal behavior of film thickness as a function of the capillary number across different morphologies. Our model aligns well with observed transitions between wimple and dimple shapes, offering valuable insights for the design of nanostructured surfaces.

Contents

* Corresponding author.
E-mail address: lorenzo.lombardi@unina.it (L. Lombardi).

https://doi.org/10.1016/j.jcis.2024.12.157
Received 12 November 2024; Received in revised form 17 December 2024; Accepted 19 December 2024

Available online 24 December 2024

1. Introduction

Thin liquid films (TLFs) are ubiquitous in a diverse range of systems and applications, including foams [1,2], emulsions [3], coatings [4], healthcare [5,6], optics [7], biosensors [8,9] and solar cells [10,11]. Free-standing films, situated between two fluid phases, can be investigated using tools such as a Sheludko cell or similar apparatus [12–14]. TLFS patterning plays a critical role in applications involving surface dewetting. Extensive research has been conducted to understand the fundamental principles that govern their behavior [15,16].

In the case of free-standing films (i.e., those situated between plateau borders in a foam), studies have shown that intricate TLF morphologies, characterized by non-uniform thickness, can significantly reduce film drainage time and thus foam lifetime [17–19]. The morphology of TLFs can be actively controlled during their formation. Various shapes of films have been documented and discussed in the literature, including *pimple*, *dimple*, *wimple*, and *ripple* [20,21]. In addition to the well-studied dimple shape, which has been extensively covered by numerous studies [1,22,23], research efforts have also focused on gaining a fundamental understanding of the wimple formation and evolution [24–26].

A well-established technique for creating free-standing TLFs and investigating their dynamics is the rising bubble experiment. In this approach, a single bubble that rises through a bulk liquid creates a TLF between its apex and the surrounding air-liquid interface [27]. The bubble may either rise freely within the bulk [2,28] or be pinned to a moving capillary to maintain a specific velocity [22,24].

The latter technique has been recently adopted to create the first example of free-standing film with a wimple morphology [24]. This was achieved by pressing an air bubble against an air-water interface through two consecutive motions at constant velocity, separated by a pause. During the first motion, a small film formed, and during the second motion, the film radius increased, resulting in a curved wimpled film. These experiments demonstrated that for a given h_0/R, there exists a critical capillary number, $Ca_w \sim (h_0/R)^2$, beyond which a wimple forms. Here $Ca_w = \eta V/\gamma$, and η denotes the liquid bulk viscosity, γ the surface tension, V the bubble approach velocity, h_0 the thickness of the initial thin film, and R the bubble radius. The wimple was observed only in films with interfacial stresses, such as those containing surfactants or surface active molecules.

While the two-step technique yields accurate and reproducible results, it does not capture the complexity of natural phenomena. In reality, bubbles often display dynamic behaviors, such as growth or oscillation near a free surface, that deviate from the idealized conditions of the two-step method. For example, bubbles near a free surface in foam can contract or expand due to sudden pressure changes, significantly affecting foam structure [29]. Bubbles may also grow and oscillate near a free surface due to rainfall [30], underwater explosions [31], or the use of air guns in seabed exploration [32]. In healthcare, ultrasound-oscillated nano- or microbubbles can destroy cancer cells, enabling non-invasive cancer therapy [33]. Oscillating bubbles are additionally employed in interfacial dilatational rheometry, where a change in bubble volume compresses or dilates the interface [27]. In laboratory settings, bubbles can also contract due to accidentally induced pressure fields [34]. Therefore, a film forming between an expanding bubble and a free surface is more realistic.

As a bubble expands toward a free surface, a liquid film can be trapped between the bubble and the free surface. Subsequently, the pressure within the film increases, causing its deformation. Conversely, when the bubble retracts from the free surface, the film experiences a decrease in pressure, potentially leading to the entry of liquid and film disappearance. Similar dynamics, for free-standing TLFs, has been explored using a thin film balance, where oscillatory pressure profiles are applied at the film boundaries to mimic the approach and departure of two bubbles [35]. Nevertheless, the behavior and morphology of TLFs formed between an oscillating bubble and a free surface remain unexplored, both experimentally and theoretically.

This study aims to investigate the behavior of a free-standing film formed by an oscillating bubble near a free surface. We hypothesize that if a thin liquid film (TLF) remains present throughout the oscillation cycle, a wimple will form at the end of the process, whereas intermittent film presence will lead to dimple formation. Furthermore, we propose that wimple thickness depends solely on the capillary number, Ca, measured during film formation, regardless of whether the film is created with an imposed velocity (two-step method [24]) or by inflating the bubble against the interface. To test these hypotheses, we conducted experiments where a bubble was inflated and deflated against a free surface to simulate oscillation, then compared the resulting film with that formed using the two-step method. A comprehensive experimental set allowed us to assess the relevance of existing models to our system and provided fundamental insights into wimple-shaped film formation. A model based on lubrication theory was applied to interpret the experimental findings, enhancing our understanding of this phenomenon.

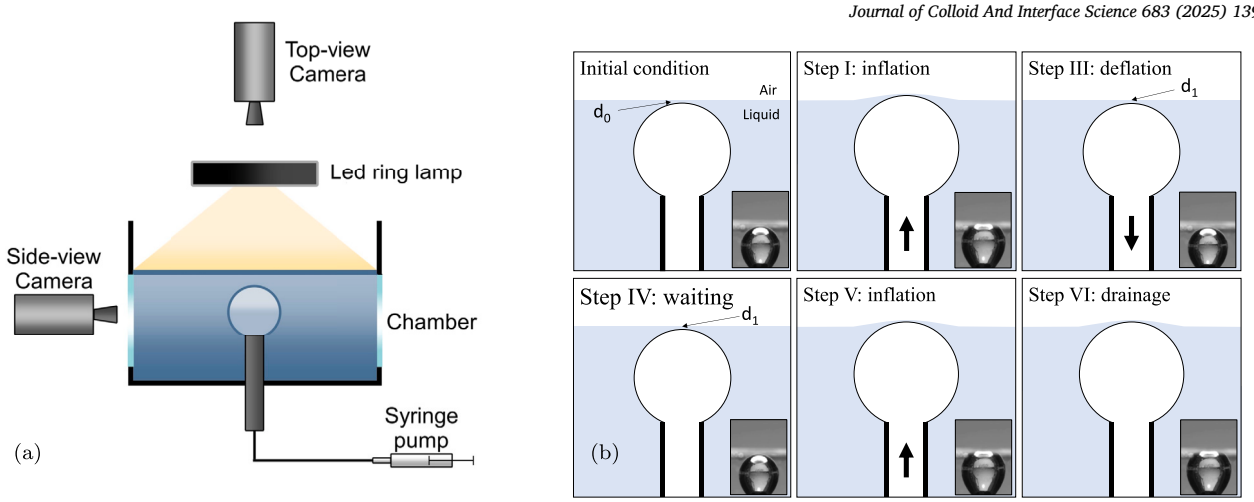

Fig. 1. (1a) Sketch of OFI setup. (1b) Sketch of bubble volume oscillation mechanism (not to scale), the insets show the bubble shape recorded from the side-view camera. Note that step ii) is omitted for brevity.

2. Materials and methods

2.1. Oscillatory fluid film interferometry setup

The oscillatory film interferometry (OFI) setup (Fig. 1a) consists of a custom black Polylactic Acid (PLA) chamber with a volume of 5.5 mL, and a 17-gauge stainless steel needle with a blunt tip (1.067 mm I.D.; 1.473 mm O.D.) on which the bubble is generated. The bubble is generated by a custom-made syringe pump [36] set in motion by a stepper motor (11 20-02D-AMT112S, NEMA, USA). A LED ring lamp (LAV-80SW2, CCS Inc, USA) is used to produce reflection interference at the fluid film interfaces, a top-view camera (Imaging Source DFK 33UX178) equipped with a telecentric lens (Edmund 0.6x TML Silver) captures interferometry images, and a side-view camera (ThorLabs sCMOS Camera) equipped with a telecentric lens (Edmund 2x TML Gold) is adopted for geometric bubble measurement. Black PLA was chosen to avoid undesired light reflections. The chamber was built with two lateral slots to accommodate two glass slides permitting the side view. A compartment at the bottom is used to place a rubber seal to avoid liquid leakage.

The chamber is fixed to a micrometric translation stage to control the distance between the needle and the air-liquid interface. The blunt needle is connected *via* high-pressure tubing (IDEX PEEK 1/16 OD″ × 0.030″ ID 1533L) to a 1 ml syringe assembled on the pumping system. The length of connections is kept as short as possible to minimize dead volume and reduce the effect of air compressibility [37]. A script was developed to allow complete automation of the entire experiment and minimize human error. The stepper motor running the syringe pump, connected to a microcontroller board (BIGTREETECH SKR Mini E3 V3.0), is controlled by a custom-made Matlab script to achieve an oscillation of the bubble toward the interface.

2.2. Surfactant solutions

Bovine Serum Albumin (BSA) and Sodium Dodecylsulfate (SDS) were chosen as surfactants for our experimental campaign. Previous studies suggest that interfacial stresses, and thus the presence of surfactants, are essential for wimple formation [24]. SDS is a largely studied anionic surfactant with no detectable interfacial viscosity [38,39], but interfacial stresses may arise due to surface tension gradients. Such stresses can trigger solutocapillary Marangoni flows and disrupt film axisymmetry [40]. Conversely, BSA is a protein known for its interfacial viscoelasticity [41]. When dissolved in water, this protein adsorbs at the air-liquid interface, forming a multilayer network [42,43]. While viscoelasticity itself does not affect film shape or drainage dynamics [34], the non-zero interfacial viscosity is a primary source of interfacial stress. At BSA-covered interfaces, the entanglement of protein molecules prevents Marangoni flows, thereby reliably preserving film axisymmetry. We conducted experiments with both surfactants to investigate the variances in wimple formation via bubble oscillation within these two systems.

BSA with a molecular weight of 66 kDa was acquired from Sigma Aldrich (catalog number: A7906, CAS: 9048-46-8, purity ≥98%). To achieve a solution concentration of 20 mg/mL, BSA lyophilized powder was dissolved in deionized water (PBS 1x from Corning Cellgro, catalog number: 21-040-CV). SDS obtained from Invitrogen Life Technologies was utilized to prepare a 20 mg/mL solution by dissolving it in deionized water. After gentle stirring, the BSA solution was aged for 30 min, i.e. until the rheological properties of BSA interfaces stop changing significantly [34,44].

Surface tension measurements for the BSA and SDS solutions at the specified concentrations resulted in $\gamma = 47$ mN/m [44] and $\gamma = 32$ mN/m [22] respectively. The bulk viscosities (η) of the BSA and SDS solutions under scrutiny are about 1.2 mPa · s [34,45,46] and 1.1 mPa · s [47,48] respectively. All experimental procedures were conducted at 25 °C.

The Boussinesq number for the BSA solution, given by $Bq = \eta_s/(\eta R_f)$ [49], is on the order of $O(10^3)$, indicating significant interfacial viscosity, where η_s represents the interfacial viscosity [41] and R_f the TLF radius. In contrast, for the SDS solution, the Boussinesq number is approximately $O(10^{-2})$, suggesting negligible interfacial viscosity.

2.3. Experimental procedure

An air bubble with radius $R = 1.46 \pm 0.07$ mm is generated from the needle tip. The bubble volume is monitored for several minutes to ensure a steady state before measuring the distance between the apex of the bubble and the air-liquid interface d_0 which is varied in the range 0.08-0.3 mm. Eventually, the oscillation protocol begins. The following six steps in series are imposed:

i) Inflation of the bubble occurs at a flow rate Q_{inf1} for a duration of t_{inf1}, establishing a liquid film between the interfaces.
ii) A very short pause for a duration of $t_{pause1} \ll t_{inf1}$.
iii) Deflation of the bubble at a flow rate Q_{def} for a period of t_{def}.
iv) The syringe remains steady for a duration of t_{pause2}.
v) A second inflation at a flow rate Q_{inf2} for a time t_{inf2}.
vi) The syringe is maintained steady until bubble coalescence.

Steps iii) and v) are executed with two different policies: one resulting in significant separation between the air-liquid interfaces at the end of step iii), denoted as Large Deflation (LD); the other, conversely, resulting in a smaller separation between the two interfaces, termed Small Deflation (SD). Essentially, these approaches vary in the duration of bubble deflation and second inflation. Specific parameter values are provided in the SI. The standard oscillation procedure is depicted in Fig. 1b.

2.4. Fluid film thickness measurement

Light interference theory is exhaustively described in literature [2,12]. Additional information on the theory and calibration used for the interferometric analysis of the film thickness is given in the SI. The film thickness map reconstruction was manually achieved through a custom developed Python software [22]. This manual matching process introduces errors in film thickness of approximately ±15 nm, estimated based on the spacing between distinguishable color bands in the color map.

2.5. Rate of evaporation measurement

To measure the rate of water evaporation from the OFI chamber under our conditions, the water level was recorded over a 30-minute period with the side-view camera. Data points were then linearly fitted to determine the evaporation rate.

3. Results and discussion

3.1. Effect of deformation history on film morphology

The observed film dynamics are presented in terms of film thickness at the center and film radius in Fig. 2b and Fig. 2c, respectively, for the BSA/water system. As the durations of steps iii), iv), and v) differ between LD and SD, establishing a common time reference is essential for comparing experiments. Time is scaled based on the moment when the film radius ceases to increase at the end of step v) (Fig. 2c). Positive times indicate exclusively film drainage during phase vi).

The progression of the film unfolds as follows, and is schematized in the sketch in Fig. 2a. In step i), a dimple forms (observed at early times in both Fig. 3a and Fig. 3b) under both forcing conditions. In step ii), the dimple remains stable, and because the pause duration is shorter than inflation duration ($t_{pause1} \ll t_{inf1}$), the film thickness can be assumed to stay constant throughout this step. In steps iii) and iv), the two policies diverge. Under LD, the separation between the interfaces becomes so substantial that the film disappears, and the system returns to its initial state (prior to step i)). Subsequent inflation follows a similar dynamic, culminating once more in dimple formation (Fig. 3b). Conversely, under SD, a small film with a radius of approximately 100μm persists until the final stages of step iv). This results in the formation of a wimple during step v). It is evident that, in the presence of a wimple, the center thickness during steps v) and vi) is significantly smaller than in the case of dimple (Fig. 2b). In both cases the film drains until bubble coalescence during step vi).

In the SD scenario, interferometry data during steps v) and vi) reveal the establishment of a stable wimple, as illustrated in Fig. 3a. In the presence of the wimple, two local thickness minima are evident (considering only half of the film extent): one near the film edge and another at the center. The film thickness at both these locations steadily decreases until reaching a stable value 50 ± 15 nm before coalescence. Interference colors corresponding to these regions indicate the presence of a "black film," likely predisposing those areas to rupture. Conversely, the maximum film thickness decreases steadily until bubble coalescence. The decrease of the maximum film thickness is also observed for the dimple formed after LD deformation, as shown in Fig. 3b. However, in this case, only one local minimum near the film edge is present, diminishing until stabilizing at the "black film". The thickness maximum is located at the center and decreases steadily until bubble coalescence.

3.2. Influence of evaporation on film morphology

Prior research reported that at long times the wimple turns into a dimple as a result of a pressure gradient pushing toward the film center [24,25]. This is because the liquid flows towards the central region, causing a localized increase in thickness. The time taken for this evolution decreases as the capillary number (Ca) increases [24].

In the current setup, the chamber remains open, unlike in previous studies [24]. As shown in Fig. 3a, we observe that the wimple shape is present until bubble coalescence. Since evaporation steadily thins the film over time, it causes the central thickness to decrease rather than increase, inhibiting wimple evolution into a dimple.

To clarify the effect of evaporation, we examine the minimum film thickness (h_{min}) over time. Previous analyses have shown that for a liquid film between two drops (in the case of a high drop-to-film viscosity ratio, $\lambda \gg 1$, which corresponds to films with immobile interfaces), the minimum film thickness scales as $h_{min}/R \sim \tau^{-2/3} Ca^{1/3}$ [23,50]. Here, the dimensionless time is defined as $\tau = t/t_c$, where $t_c = \eta R/\gamma$ is the viscocapillary time. This scaling has been validated for free-standing films with immobile interfaces [2].

The capillary number ($Ca = \eta V/\gamma$) is determined by the vertical component of the velocity at which the bubble approaches the free surface (V). This is a function of radial position r, bubble radius $R(t)$, and inflation flow rate Q, which is imposed. In the final stages of motion, when the film is formed, the relative change in R over time is about 0.1%, making it negligible. The radial extent of the film amounts to less than 30% of R. By simple geometric analysis, this leads to a maximum decrease of V across R_f of approximately 5%. Following these considerations, we regarded V as invariant with respect to r across R_f.

The actual flow rate and the motion time may vary slightly from the imposed values due to air compressibility and the presence of dead volume in the tubes and capillaries used for bubble inflation, which can lead to volume instabilities and inflation delays [37]. As a result, estimating V based solely on the imposed flow rate is challenging. An alternative approach is to measure V by tracking the bubble profile from a lateral view. Yet, when the bubble surface nears the free surface during film formation, the distinction between the two interfaces is made difficult by light diffraction, complicating accurate velocity measurements from the lateral view. A better method involves indirectly measuring V by assessing the rate of increase in film radius R_f during phase v). Under the previous assumptions, the bubble may be treated as a sphere advancing toward the free surface at velocity V, equivalent to the rate of increase of R_f.

The rate of increase in R_f is determined by the slope of the line fitted to data points in Fig. 2c obtained during phase v). Across various experiments with different flow rates, the velocity (V), during the second inflation, ranges from 20 to 200 μm/s due to the variability of R, leading to Ca ranging between $7 \cdot 10^{-7}$ and $7 \cdot 10^{-6}$. Applying the h_{min} scaling allows us to collapse data for BSA in cases of wimple and dimple formation, confirming the scaling accuracy, as shown in Fig. 4. However, data deviates from the $-2/3$ power law at around $\tau Ca^{-1/2} \approx 2 \cdot 10^7$, where the film thickness decreases more steeply. In this later stage, data follows a power law of approximately -1, which significantly diverges from the predicted $-2/3$. This behavior, consistent with previous studies [2,51], is likely due to the effect of evaporation. A comparison between the data obtained under suppressed evaporation conditions and those with evaporation is provided in the SI.

Typically, the rate of evaporation is not constant over time as it varies with the water mole fraction within the film [52]. Due to the significantly larger molecular weight of BSA ($6.6 \cdot 10^4$ g/mol) compared to water, at our chosen concentration, the mole fraction of BSA in the solution tends to zero throughout most of the drainage process. This applies until the final stages of drainage just before coalescence, when the water is almost completely evaporated and the black film becomes visible. At such a thin thickness, around 50 ± 15 nm, the film primarily comprises BSA proteins with minimal water content, leading to negligi-

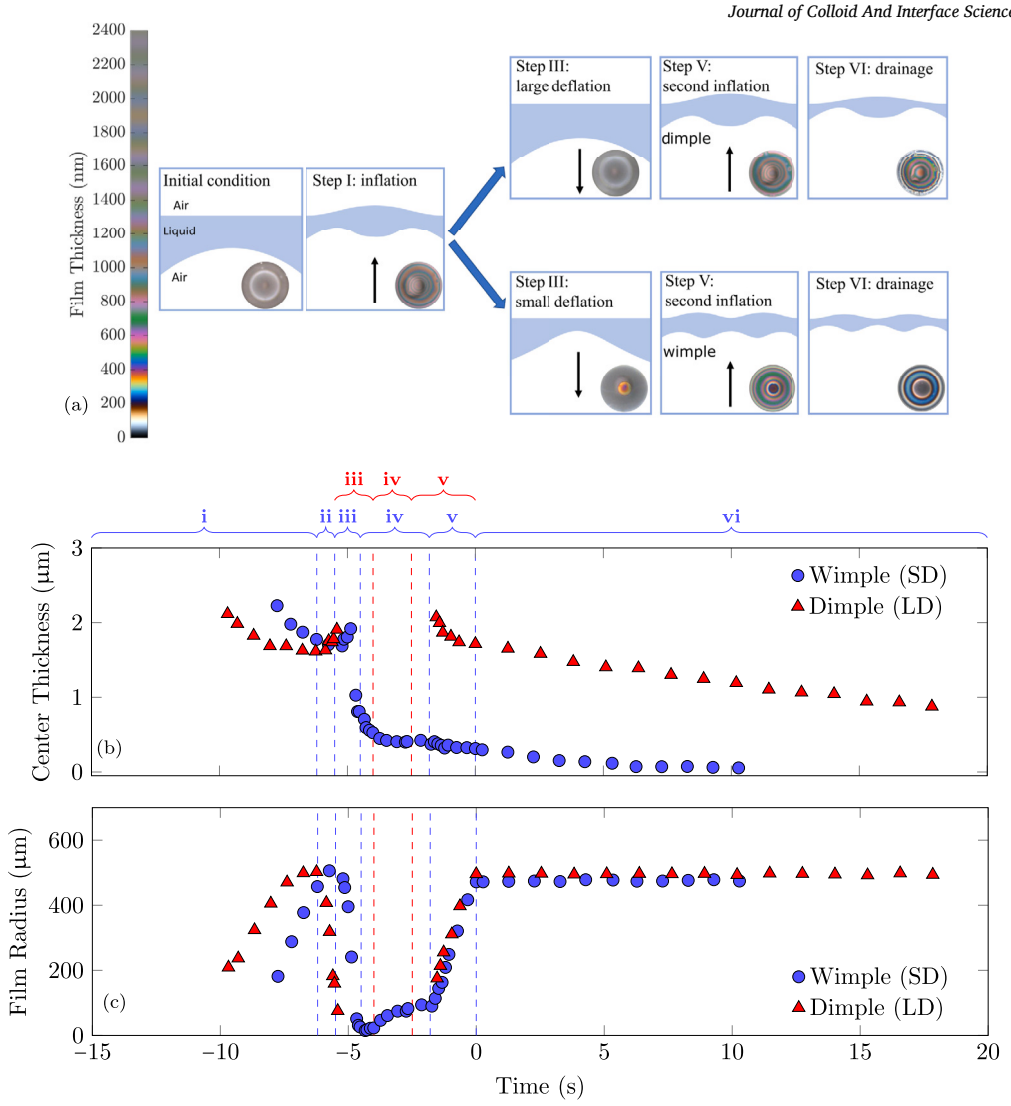

Fig. 2. (2a) Sketch of thin liquid film evolution during the six steps of the experiments (the sketch is not to scale and represents the film centerline). The film adopts different conformations depending on whether a film is present before the second inflation. The sketches related to pauses (ii) and iv)) are omitted for clarity. Experimentally obtained interferograms for the corresponding cases are shown below. (2b) Time evolution of film thickness at the center for BSA solution for two different positions before second inflation. (2c) Radial extent of the thin liquid film as a function of time for BSA solution for two different positions before second inflation.

ble evaporation. Thus, the evaporation rate can be assumed to remain constant until the final stages of drainage. The experimentally measured evaporation rate is approximately 40 nm/s (as reported in the SI).

3.3. Effect of SDS on film morphology

Comparable experiments to those conducted with BSA have been executed utilizing SDS. Similarly to the observations with BSA, the presence of SDS during the SD procedure causes the persistence of a tiny film in phase iv). This results in the emergence of a wimple structure in phase v) which subsequently drains during phase vi). This is in agreement with previous observations regarding the ability to induce wimple morphology with a molecule like SDS, which lacks interfacial viscosity but presents concentration gradients as the source of interfacial stresses [24]. In the case of LD, similar to BSA, no film is observed during phase iv), leading to the subsequent formation of a dimple in phase v).

The primary distinction between the film morphology formed with BSA and SDS is in the film axisymmetry observed during phase vi). In the case of BSA, the film maintains perfect axisymmetry throughout phase vi) (Fig. 3), whereas a loss of symmetry occurs after the second inflation in the presence of SDS (Fig. 5). This phenomenon is attributed to solutocapillary Marangoni flows, which, by pulling the liquid toward the center of the film, induce abrupt instabilities [24,40]. Detailed quantitative results regarding the axisymmetry of the films produced in this study are provided in the SI.

3.4. Numerical model

In order to elucidate the mechanism of wimple or dimple formation we have utilized a simple 1D model based on the lubrication theory [20] and accounting for evaporation. The model is derived applying the condition of tangentially immobile interfaces and assuming that the film drainage is axisymmetric. The model has been implemented in COMSOL Multiphysics® and solved using a finite element method. Gravity can be considered negligible since $Bo = \rho|g|R^2/\gamma < 1$ where ρ is the liquid density, and g is the acceleration due to gravity. In the experimental system under consideration $Re = \rho V h/\eta \ll 1$ and $We = CaRe \ll 1$. Consequently, inertia is insignificant compared with viscous and surface tension forces. The non-dimensional Stokes-Reynolds film drainage equation reads as follows [20] (non-dimensional variables are denoted with prime):

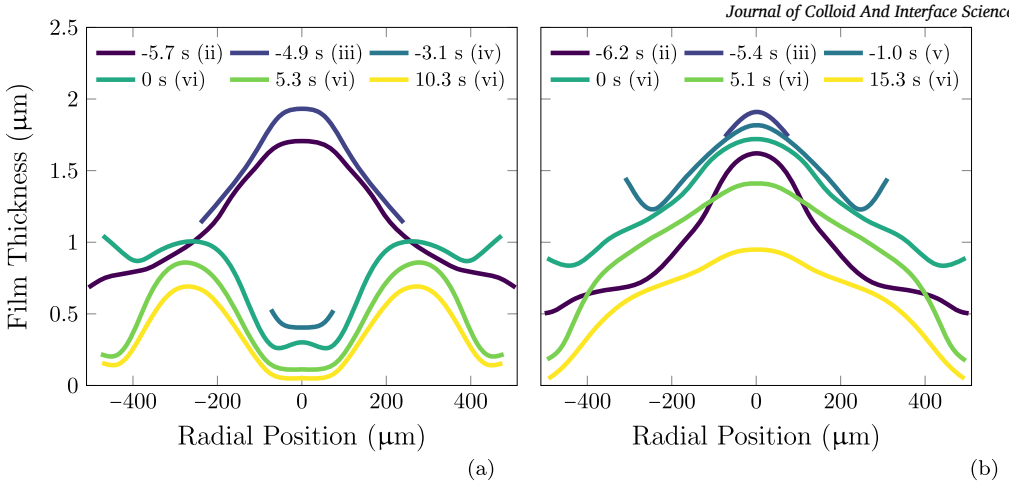

Fig. 3. (3a) Interferograms of thin BSA films illustrating the evolution of film thickness with a film present at the start of the second inflation, leading to wimple formation. The parameters used in the experiment are: $d_0 = 100$ μm, $Q_{inf1} = 10$ mm^3/s, $t_{inf1} = 1$ s, $t_{pause1} = 0.5$ s, $Q_{def} = 15$ mm^3/s, $t_{def} = 0.5$ s, $t_{pause2} = 2$ s, $Q_{inf2} = 10$ mm^3/s, $t_{inf2} = 2.5$ s. (3b) Interferograms of thin BSA films illustrating the evolution of film thickness without a film present at the start of the second inflation, leading to dimple formation. The parameters used in the experiment are: $d_0 = 100$ μm, $Q_{inf1} = 10$ mm^3/s, $t_{inf1} = 1$ s, $t_{pause1} = 0.5$ s, $Q_{def} = 15$ mm^3/s, $t_{def} = 1$ s, $t_{pause2} = 1.5$ s, $Q_{inf2} = 10$ mm^3/s, $t_{inf2} = 2.5$ s. The BSA concentration is 20 mg/ml. The time is shifted so that zero corresponds to when the film radius is no longer increasing at the end of second inflation. The radial thickness profiles are taken along the vertical centerline.

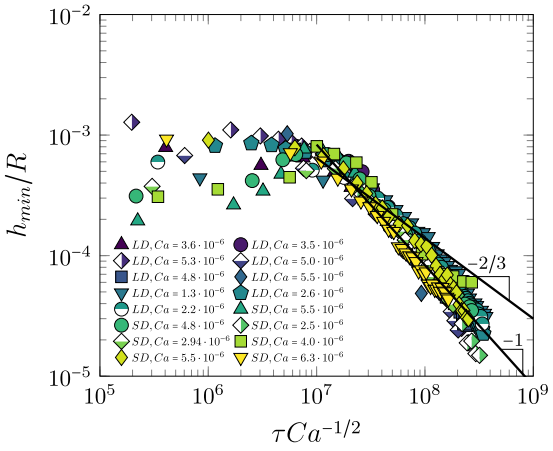

Fig. 4. Minimum film thickness scaled with bubble radius as a function of non-dimensional time rescaled by $Ca^{-1/2}$ for BSA experiments. Note that here the time is shifted so that $\tau = 0$ correspond to the start of the second inflation.

$$\frac{\partial h'}{\partial t'} = \frac{1}{12r'}\frac{\partial}{\partial r'}\left(r' h'^3 \frac{\partial p'}{\partial r'}\right) - E'. \tag{1}$$

Here p' is the pressure, and E' is a Heaviside-like function of film thickness h', based on the assumption that the evaporation rate remains constant until the thickness reaches a critical value $h'_{E'_0}$, at which evaporation ceases (see Section 3.2). It is defined as $E' = E'_\infty/(1+\exp(-a'(h' - h'_{E'_0})))$ where E'_∞ is the non-dimensional evaporation rate, and a' is chosen so that $1/a' \ll h'_{E'_0}$ to have a steep decrease in E' when $h' = h'_{E'_0}$. Evaporation rate data are reported in SI.

The non-dimensional Young-Laplace equation for two approaching bubbles reads:

$$\frac{\partial}{\partial r'}\left(r'\frac{\partial h'}{\partial r'}\right) = 2r'(2 - \Pi' - p'). \tag{2}$$

The disjoining pressure Π' is set to zero, as it remains negligible until the film thickness reaches approximately 20 nm, for BSA concentrations both below and above that used in this work [53,54]. The non-dimensional boundary and initial conditions are the following:

$$\text{I.C.: } h'(0, r') = h'_0 + r'^2;\ p'(0, r') = 0, \tag{3}$$

$$\text{B.C.: } \frac{\partial p'}{\partial r'} = 0; \quad \frac{\partial h'}{\partial r'} = 0 \quad \text{at } r' = 0, \tag{4}$$

$$\text{B.C.: } p' = 0 \quad \text{at } r' = Ca^{-1/4}. \tag{5}$$

An additional boundary condition is required to define the motion history:

$$\text{B.C. : } \frac{\partial h'}{\partial t'} = \begin{cases} V'_1, & 0 \le t' < t'_1 \\ V'_2, & t'_1 \le t' < t'_2 \\ V'_3, & t'_2 \le t' < t'_3 \\ V'_4, & t'_3 \le t' < t'_4 \\ V'_5, & t'_4 \le t' < t'_5 \\ V'_6, & t'_5 \le t' < t'_6 \end{cases} \quad \text{at } r' = Ca^{-1/4} \tag{6}$$

The derivation of the non-dimensional governing equations, along with the initial and boundary conditions, is provided in the SI. The capillary number $Ca = \eta V/\gamma$ corresponds to the second bubble inflation.

The scaling parameters used for non-dimensionalization are the following: $\bar{h} = Ca^{1/2}R_o$ (film thickness), $\bar{r} = Ca^{1/4}R_o$ (radial coordinate), $\bar{t} = Ca^{1/2}R_o/V$ (time), $\bar{p} = \gamma/R_o$ (pressure). Here, $R_o = 2/(1/R_{1o} + 1/R_{1o})$ is the equivalent bubble radius, with R_{1o} being the undeformed bubble radius, and $R_{2o} \to \infty$.

As shown in Equation 6, the implemented motion history unfolds as follows: i) the bubble moves toward the surface, ii) a pause follows, iii) the bubble retreats from the free surface, iv) another pause follows, v) the bubble is once more pushed towards the free surface, and vi) the bubble is steady until the end of the simulation. Two distinct scenarios have been analyzed, differing only in step iii): small retraction (SR) and large retraction (LR). These are the equivalent of the experimental procedures SD and LD, respectively.

In both cases the model predicts the formation of a dimple at the end of step i) as shown in Fig. 6. In the SR case, the results show the formation of a wimple during step v) (Fig. 6a). The wimple is visible throughout the entire film drainage phase vi) as in the experiments. On the other hand, in the LR case, the results show the formation of a dimple in step v) as shown in Fig. 6b.

The model is particularly useful for visualizing the film shape at thicknesses greater than 2 μm, which are not accessible through our interferometry technique. Additionally, it offers pressure profiles within the film. In the LD experiments, the bubble surface recedes from the free surface until the interference color become no longer visible, indicating the absence of a film. This aligns with $t' = -150$ in the simulation re-

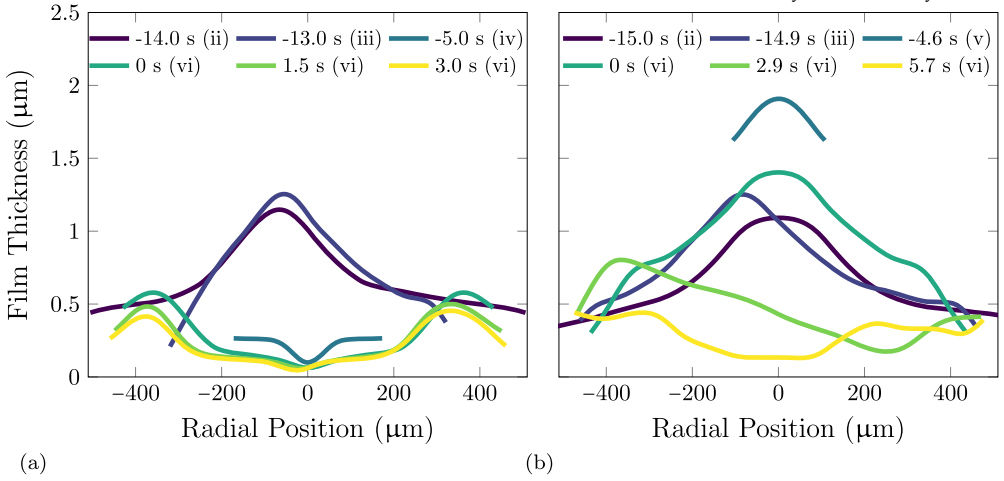

Fig. 5. (5a) Interferograms of thin SDS films illustrating the evolution of film thickness with a film present at the start of the second inflation, leading to wimple formation. The parameters used in the experiment are: $d_0 = 100$ μm, $Q_{inf1} = 10$ mm^3/s, $t_{inf1} = 1$ s, $t_{pause1} = 0.5$ s, $Q_{def} = 15$ mm^3/s, $t_{def} = 0.5$ s, $t_{pause2} = 2$ s, $Q_{inf2} = 10$ mm^3/s, $t_{inf2} = 2.5$ s. (5b) Interferograms of thin SDS films illustrating the evolution of film thickness without a film present at the start of the second inflation, leading to dimple formation. The parameters used in the experiment are: $d_0 = 100$ μm, $Q_{inf1} = 10$ mm^3/s, $t_{inf1} = 1$ s, $t_{pause1} = 0.5$ s, $Q_{def} = 15$ mm^3/s, $t_{def} = 1$ s, $t_{pause2} = 2$ s, $Q_{inf2} = 10$ mm^3/s, $t_{inf2} = 2.5$ s. The SDS concentration is 20 mg/ml. The time is shifted so that zero corresponds to when the film radius is no longer increasing at the end of second inflation. The radial thickness profiles are taken along the vertical centerline.

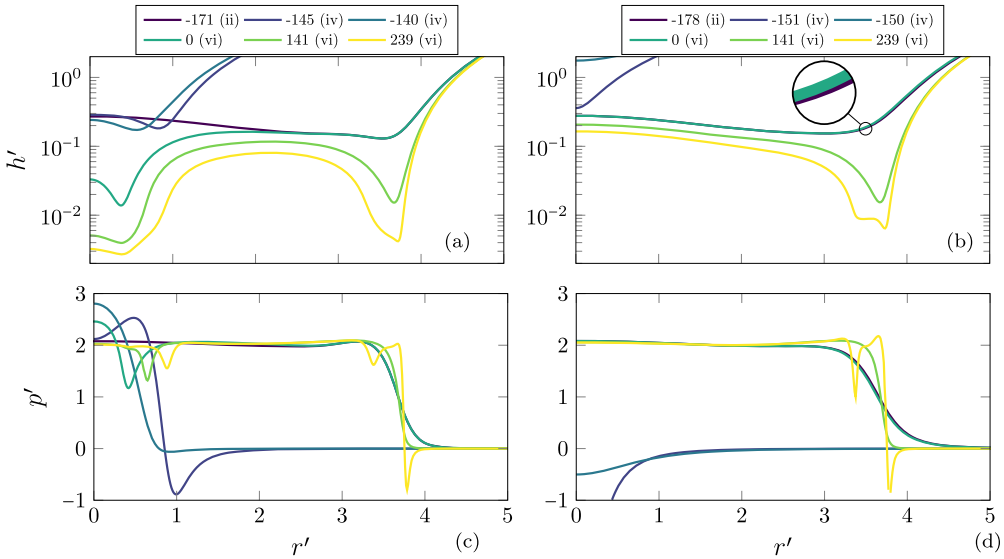

Fig. 6. (6a and 6b) Radial non-dimensional film thickness profiles from numerical simulations showing wimple and dimple formation, respectively. (6c and 6d) Radial non-dimensional pressure profiles from numerical simulations for wimple and dimple formation, respectively. The time is shifted so that the zero corresponds to the end of the last motion. Note that the pressure never drops to zero, at $r' = 0$, in the case of wimple formation, unlike in dimple formation. The inset shows overlapping curves at non-dimensional times of -131 and 0. The values of the simulations parameters are reported in SI.

sults (Fig. 6b), where the minimum distance between the bubble and the free surface is quite larger than the thickness of the first formed dimple ($t' = -178$).

In both scenarios, as shown in Fig. 6c and Fig. 6d, once the film is fully formed (steps v and vi), the pressure along the film stabilizes at a plateau equivalent to the non-dimensional Laplace pressure within the bubble ($p' = 2$). Subsequently, the pressure gradually decreases towards the bulk liquid pressure $p' = 0$. In the SR scenario (Fig. 6c), excluding the early times when motion begins, there exists a consistent radial coordinate where $p' \approx 2$. This is a necessary condition for film existence. Conversely, if the bubble retreats sufficiently from the free surface (Fig. 6d), pressure uniformly reaches zero ($p' \approx 0$), matching the bulk pressure, indicating the absence of any film. It follows that when the bubble approaches the free surface when a film is already present, a wimple forms. While, if the bubble approaches the surface with no pre-existing film, a dimple identical in thickness and pressure, to that formed after the first motion is visible.

To compare the simulation results with the experimental data, we conducted simulations for SR and LR using the experimental capillary numbers: $Ca = 4 \cdot 10^{-6}$ and $Ca = 4.8 \cdot 10^{-6}$, respectively. As shown in Fig. 7, there is excellent agreement between the experimental and simulation results. In the case of wimple formation (Fig. 7a), the simulation accurately captures the formation of a small dimple at the center, which is barely visible in the experiments due to the resolution limitations of the interferometric technique. The simulation results also reveal that the film shape is radially resolved beyond what the experimental reconstruction shows. The thickness gradient in that region is so steep that the experimentally measured thickness quickly exceeds the detection threshold for interferometric color measurement.

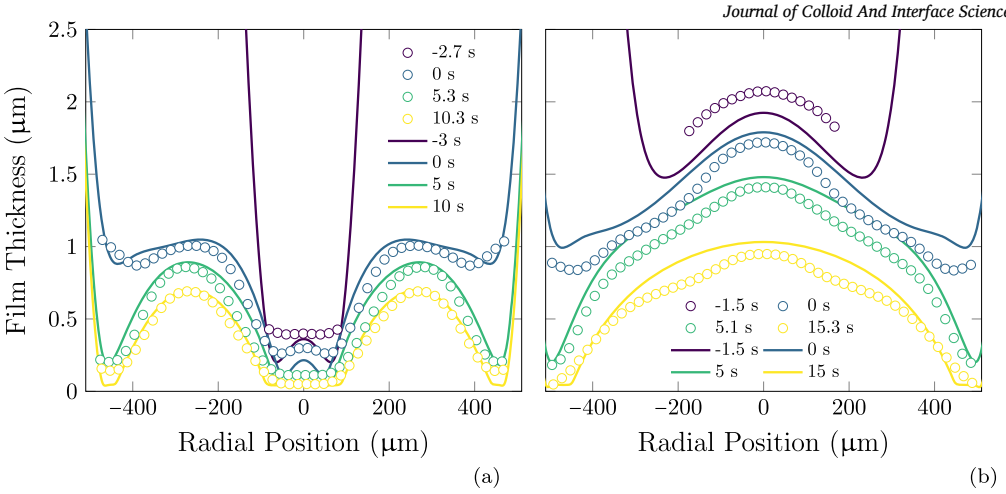

Fig. 7. (7a) Comparison between experimental (circles) and computed (lines) film thickness profiles in the case of wimple formation during the last inflation ($Ca = 4 \cdot 10^{-6}$). The parameters used in the experiment are: $d_0 = 100$ μm, $Q_{inf1} = 10$ mm^3/s, $t_{inf1} = 1$ s, $t_{pause1} = 0.5$ s, $Q_{def} = 15$ mm^3/s, $t_{def} = 0.5$ s, $t_{pause2} = 2$ s, $Q_{inf2} = 10$ mm^3/s, $t_{inf2} = 2.5$ s. (7b) Comparison between experimental (circles) and computed (lines) film thickness profiles in the case of dimple formation during the last inflation ($Ca = 4.8 \cdot 10^{-6}$). The parameters used in the experiment are: $d_0 = 100$ μm, $Q_{inf1} = 10$ mm^3/s, $t_{inf1} = 1$ s, $t_{pause1} = 0.5$ s, $Q_{def} = 15$ mm^3/s, $t_{def} = 1$ s, $t_{pause2} = 2$ s, $Q_{inf2} = 10$ mm^3/s, $t_{inf2} = 2.5$ s. The time is shifted so that zero corresponds to when the film radius is no longer increasing at the end of second inflation. The values of the simulations parameters are reported in SI.

3.5. Effect of Ca on film thickness

The theoretical prediction for the mean film thickness h_m as a function of Ca indicates that $h_m/R \sim Ca^{1/2}$ [55]. This scaling has already been validated in the case of a free-standing film exhibiting a wimple morphology [24]. It has also been demonstrated that this scaling holds for quasistatic collisions across various experimental systems [56], such as bubbles in water interacting with a glass surface, ethanol drops in air colliding with a glass surface, and mercury drops in water colliding with a mica surface.

The scaling arises from analyzing the pressure within a film situated between a sphere and a flat solid surface, as the sphere moves toward the surface at a constant velocity V. Assuming zero tangential velocity at the boundaries, the pressure follows the relation $P \sim \eta V R/h^2$ [55], where h is the minimum distance between the sphere and the free surface. As the bubble nears the free surface, the film pressure approaches the magnitude of the Laplace pressure, $O(\gamma/R)$, causing the bubble to deform.

In this scaling, it is implicitly assumed that the entire film volume contributes to bubble deformation as the bubble approaches the free surface. However, this assumption is not valid in the case of wimple formation. In that scenario, a small, flat film is already present before the second deformation begins. Since the pressure in the film only increases outside the initial film during the second deformation (Fig. 6c), the thickness of the newly formed film is not directly related to the liquid volume in the tiny film.

Analyzing film profiles for similar Ca, it emerges that the film thickness at the periphery is nearly identical for both the wimple and dimple cases. However, at a certain radial position, the two profiles diverge—one increasing in thickness (dimple) and the other decreasing (wimple) toward the center. This deviation consistently appears near the location of maximum thickness in the wimple. Thus, we can define a pinch thickness, h_p, which corresponds to the maximum thickness at $t = 0$ s in the case of the wimple, and to the film thickness at the same position in the case of the dimple with a similar Ca. As shown in Fig. 8a, h_p scales only with R and Ca, independent of the film shape. Therefore, we can exclude the contribution of the initial tiny film on h_p.

To standardize mean thickness data across different film morphologies and surface-active species, it is possible to use a modified scaling for h_m, that accounts for the differences in film shape. Modifying the scaling adopted in [24], we define $h/\beta R \sim Ca^{1/2}$, where β is a shape factor defined as the ratio between the liquid volume in the dimple and in the deformed portion of the wimple (i.e. that formed during the second inflation), approximating both profiles as portions of a circular arc. As shown in Fig. 8b, considering the arc described by the equation $h_a(r) = \sqrt{R_f^2 - r^2} - (R_f - h_{max,d})$, where the arc maximum value equals the maximum dimple thickness $h_{max,d}$, one can define a mean thickness by integrating h_a. This is done from R_f to 0 for the dimple, and from R_f to R_i for the wimple, where R_i is the radial coordinate of the inflection point of the thickness curve between $r = 0$ and the radial position of the maximum wimple thickness, R_w. By computing the mean values and multiplying each by the base area, the following equation for β is obtained:

$$\beta = \frac{V_w}{V_d} = \frac{\frac{\pi R_f^2 - \pi R_i^2}{R_f - R_i}\int_{R_i}^{R_f} h_a\, dr}{\frac{\pi R_f^2}{R_f}\int_0^{R_f} h_a\, dr} = \frac{(R_f + R_i)\int_{R_i}^{R_f} h_a\, dr}{R_f \int_0^{R_f} h_a\, dr} \tag{7}$$

A few important points should be noted: First, the wimple is assumed to have the same thickness as the dimple from R_f to R_i, and zero thickness for $r < R_i$. Second, β is calculated using values from wimple and dimple experiments conducted at similar Ca. Consequently, $\beta = 1$ for each dimple experiment, while for the wimple, $0 < \beta < 1$. The definition of R_i is guided by the observation that the omitted wimple thicknesses for $r < R_i$ are effectively compensated by the arc height surpassing the actual wimple thickness within the range $R_i < r < R_w$ (Fig. 8b). A comparison of the wimple and dimple volumes, calculated analytically or reconstructed from the experimentally measured mean thickness, is provided in the SI.

In order to obtain a scaling for h_m the mean value for β in the case of the wimple is computed and is $\beta = 0.7 \pm 0.04$. Hence, the mean film thickness h_m at the time where R_f ceases to increase is non-dimensionalized with βR and plotted against Ca in Fig. 8c. Notably, data for both film morphologies adhere to the provided scaling. This scaling is consistent with both BSA and SDS data, underscoring its generality and indicating the equivalence of these systems in achieving wimple or dimple formation.

For comparison, Fig. 8c displays simulation data for both wimple and dimple morphologies at different Ca of the second inflation, alongside data generated using the two-motion procedure from [24] without evaporation suppression. As shown, there is a strong correlation between simulations and experiments for both film morphologies. Additionally, data obtained through the two-motion procedure exhibit considerably

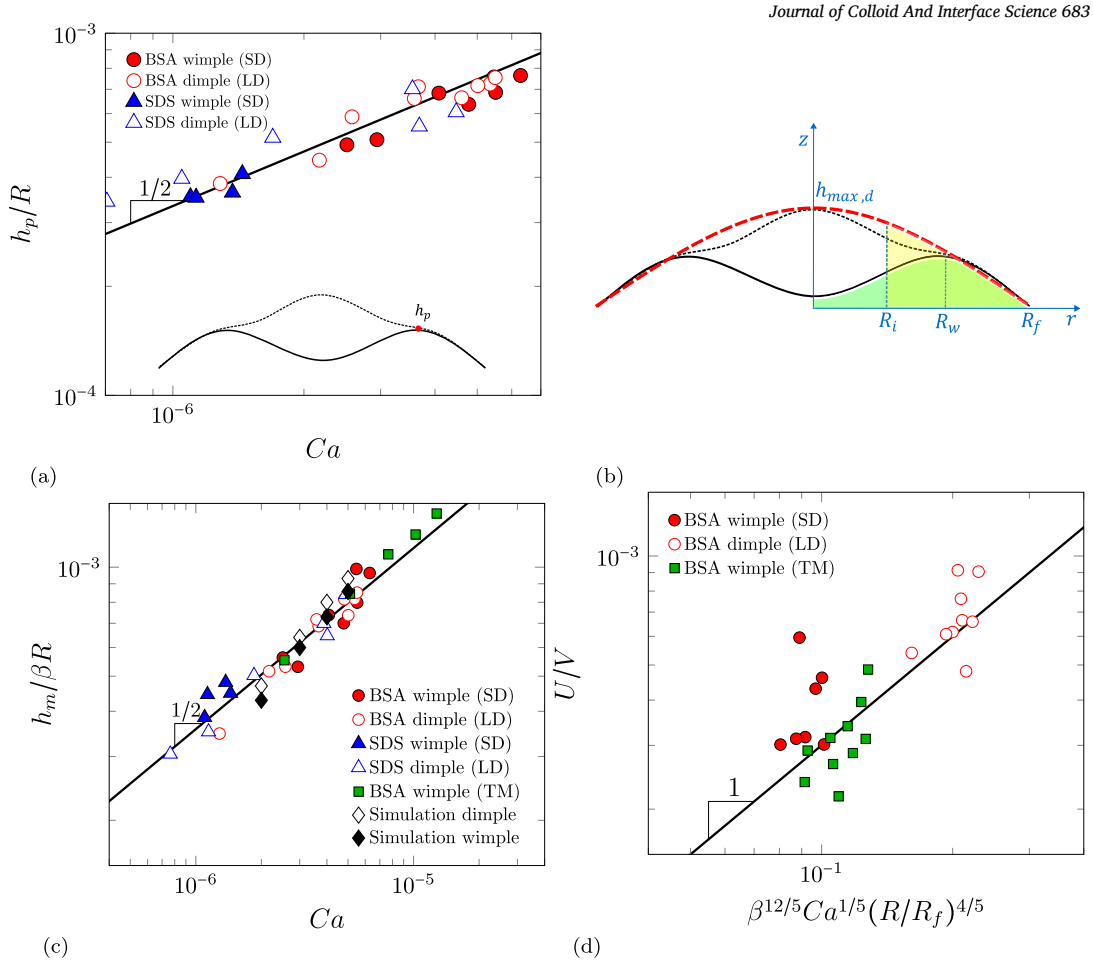

Fig. 8. (8a) Non-dimensional film pinch thickness at various Ca of the second inflation for BSA and SDS experiments with dimple or wimple morphology after the second inflation. The pinch thickness is evaluated at the radial position of the wimple maximum thickness for both film morphologies, as shown in the inset. Considering error propagation, the non-dimensional thickness error is estimated at approximately 7%. (8b) Illustration of the arc (red dashed line) approximating the dimple profile used for β estimation. Yellow highlighted area corresponds to thicknesses used in the wimple volume approximation for β calculation. Green highlighted area corresponds to the actual wimple profile. Note that the green and yellow areas partially overlap. (8c) Mean non-dimensional film thickness at various Ca of the second inflation for BSA and SDS experiments with dimple or wimple morphology after the second inflation. Considering error propagation, the non-dimensional thickness error for the inflation method is estimated at approximately 10%. Simulation data and data for BSA wimpled films generated using the two-motion procedure are included for comparison. Simulation data are obtained varying Ca of the second inflation. The values of the simulations parameters are reported in SI. Each data point for the two-step method represents the mean value from three repeats at the same imposed Ca of the second motion, with an error of less than 5%. Error bars are omitted for clarity. (8d) Non-dimensional drainage velocity as a function of Ca, film radius, and bubble radius for BSA films exhibiting wimple and dimple morphologies, constructed using both inflation and two-motions procedures. The power-law with slope 1 represents the Tsekov scaling for film drainage velocity. Data are relative to the second inflation or motion of the bubble. (For interpretation of the colors in the figure(s), the reader is referred to the web version of this article.)

less scatter than those produced with the method used in this study, confirming the former approach's higher accuracy. Nevertheless, both data sets adhere to the same scaling observed in the oscillating bubble setup, supporting our hypothesis.

As shown in Fig. 8c, all data follow the same power-law relationship $h_m\beta R = cCa^{1/2}$, where c is a constant. The literature reports that c is a very weak function of Ca, typically ranging from approximately 0.3 for $Ca \approx 10^{-10}$ to 0.5 for $Ca \approx 10^{-4}$ across various systems [20,56]. In our experiments, $c \approx 0.35$ for Ca values between 10^{-6} and 10^{-4}, consistent with the range reported in the literature.

3.6. Effect of Ca on drainage velocity

According to Tsekov theory, the drainage velocity for films with non-uniform thickness scales as [57]:

$$U = \frac{1}{6\eta}\sqrt[5]{\frac{h_m^{12}\Delta P^8}{4\gamma^3 R_f^4}}, \tag{8}$$

where ΔP is the pressure drop across the film, which when disjoining pressure is negligible, scales as $\Delta P \sim \gamma/R$. This scaling has been shown to accurately describe the transition time from wimple to dimple in the absence of evaporation [24]. Therefore, we employ a similar scaling for the drainage velocity of films with varying morphologies.

Considering that $h/\beta R \sim Ca^{1/2}$, one can derive the non-dimensional scaling as:

$$\frac{U}{V} \sim \sqrt[5]{\frac{\beta^{12}R^4Ca}{{R_f}^4}} \tag{9}$$

Examining the drainage velocity U at $t = 0$ s (when thickness is at its maximum and evaporation is negligible) for BSA films with both wimple and dimple shapes (Fig. 8d), we observe that, despite some data scatter, there is fair agreement with the scaling predicted by Tsekov theory (Equation 9). Data generated using the two-motion procedure are also included here for comparison, showing good agreement with the proposed scaling as well.

4. Conclusions

This study advances the understanding of thin liquid films (TLFs) formed between a free surface and an oscillating bubble by examining the morphology and drainage dynamics of BSA/SDS-decorated films through dynamic film interferometry, alongside a lubrication theory-based model [20]. Both experiments and simulations reveal that film morphology is significantly influenced by the deformation history: a wimple forms only if a film remains present throughout the oscillation history, while a dimple forms if the film intermittently disappears, confirming the primary hypothesis. This conclusion is further supported by the simulated film pressure profiles.

A scaling analysis demonstrates that evaporation strongly affects thin film dynamics, accelerating drainage [23]. A modified scaling approach, based on the thin-gap approximation [24,55] and incorporating the volume of films with wimple or dimple morphologies, identifies a universal behavior of mean thickness as a function of the capillary number, Ca, for films with these complex shapes. The lubrication theory model aligns well with both analytical scaling and experimental results, effectively capturing the transition between wimple and dimple morphologies as well as drainage dynamics. Additionally, experiments show that the film drainage velocity at the end of the second inflation depends on Ca, film radius, and bubble radius, following the scaling law proposed by Tsekov for films with non-uniform thickness [57].

A comparison of data from the oscillating bubble method and the two-motion technique [24] confirms that while the two-motion technique offers greater control and precision, both methods are equally effective in producing films with these morphologies, as film thickness depends solely on the Ca of the final inflation/motion, confirming the second hypothesis. The insights from this study contribute to the understanding needed to create highly ordered nanostructured surfaces. Control of film morphology at the nanoscale could facilitate the development of hierarchical materials with customized functionalities [10,58–61]. This work lays a foundation for future research aiming to develop solidified films with non-uniform morphologies.

CRediT authorship contribution statement

Lorenzo Lombardi: Writing – original draft, Validation, Software, Methodology, Investigation, Formal analysis, Data curation, Conceptualization. **Pasquale Calabrese:** Investigation. **Daniele Tammaro:** Writing – review & editing, Supervision, Investigation, Conceptualization. **Pier Luca Maffettone:** Writing – review & editing, Writing – original draft, Validation, Supervision, Resources, Project administration, Methodology, Funding acquisition, Formal analysis, Conceptualization.

Declaration of competing interest

The authors declare that they have no known competing financial interests or personal relationships that could have appeared to influence the work reported in this paper.

Appendix A. Supplementary material

Supplementary material related to this article can be found online at https://doi.org/10.1016/j.jcis.2024.12.157.

Data availability

Data will be made available on request.

References

[1] E. Chatzigiannakis, N. Jaensson, J. Vermant, Thin liquid films: where hydrodynamics, capillarity, surface stresses and intermolecular forces meet, Curr. Opin. Colloid Interface Sci. 53 (2021) 101441, https://doi.org/10.1016/J.COCIS.2021.101441.

[2] L. Lombardi, S. Roig-Sanchez, A. Bapat, J.M. Frostad, Nonaqueous foam stabilization mechanisms in the presence of volatile solvents, J. Colloid Interface Sci. (2023), https://doi.org/10.1016/j.jcis.2023.05.156.

[3] D. Langevin, Coalescence in foams and emulsions: similarities and differences, Curr. Opin. Colloid Interface Sci. 44 (2019) 23–31, https://doi.org/10.1016/J.COCIS.2019.09.001.

[4] H.J. Griesser, Thin Film Coatings for Biomaterials and Biomedical Applications, Elsevier, 2016.

[5] R.J. Braun, Dynamics of the tear film 44 (2011) 267–297, https://doi.org/10.1146/annurev-fluid-120710-101042, https://www.annualreviews.org/doi/abs/10.1146/annurev-fluid-120710-101042.

[6] V. Chandran Suja, A. Verma, E. Mossige, K. Cui, V. Xia, Y. Zhang, D. Sinha, S. Joslin, G. Fuller, Dewetting characteristics of contact lenses coated with wetting agents, J. Colloid Interface Sci. 614 (2022) 24–32, https://doi.org/10.1016/j.jcis.2022.01.075.

[7] J. Oliver, T. Kessler, H. Huang, J. Keck, A. Rigatti, A. Schmid, A. Kozlov, T. Kosc, Thin-Film Design for Multilayer Diffraction Gratings, 2005, p. 59911A.

[8] C. Di Natale, S. Russo, F. Graziano, V. Vespini, G. Luciani, G. Vitiello, L. Lombardi, F. Ferranti, S. Mari, P. Luca Maffettone, S. Grilli, S. Coppola, P. Ferraro, Sensitive colorimetric immunosensor using AuNP-functionalized polymer film for picogram-level detection of Tau protein intermediate aggregates, J. Colloid Interface Sci. 678 (2025) 1052–1059, https://doi.org/10.1016/J.JCIS.2024.08.201.

[9] S. Prakash, T. Chakrabarty, A.K. Singh, V.K. Shahi, Polymer thin films embedded with metal nanoparticles for electrochemical biosensors applications, Biosens. Bioelectron. 41 (2013) 43–53, https://doi.org/10.1016/J.BIOS.2012.09.031.

[10] Z. Yu, A. Raman, S. Fan, Fundamental limit of nanophotonic light trapping in solar cells, Proc. Natl. Acad. Sci. USA 107 (2010) 17491–17496, https://doi.org/10.1073/PNAS.1008296107/SUPPL_FILE/PNAS.1008296107_SI.PDF, https://www.pnas.org/doi/abs/10.1073/pnas.1008296107.

[11] Z. Saki, M.M. Byranvand, N. Taghavinia, M. Kedia, M. Saliba, Solution-processed perovskite thin-films: the journey from lab- to large-scale solar cells, Energy Environ. Sci. 14 (2021) 5690–5722, https://doi.org/10.1039/D1EE02018H, https://pubs.rsc.org/en/content/articlehtml/2021/ee/d1ee02018h, https://pubs.rsc.org/en/content/articlelanding/2021/ee/d1ee02018h.

[12] A. Sheludko, Thin liquid films, Adv. Colloid Interface Sci. 1 (1967) 391–464, https://doi.org/10.1016/0001-8686(67)85001-2.

[13] L.G. Cascão Pereira, C. Johansson, H.W. Blanch, C.J. Radke, A bike-wheel microcell for measurement of thin-film forces, Colloids Surf. A, Physicochem. Eng. Asp. 186 (2001) 103–111, https://doi.org/10.1016/S0927-7757(01)00488-5.

[14] V. Ferraro, M. Villone, V. Tkachenko, L. Miccio, L. Lombardi, D. Tammaro, E. Di Maio, G. D'Avino, P. Maffettone, Axisymmetric bare freestanding films of highly viscous liquids: preparation and real-time investigation of capillary leveling, J. Colloid Interface Sci. 596 (2021), https://doi.org/10.1016/j.jcis.2021.03.102.

[15] A. Sharma, R. Khanna, Pattern formation in unstable thin liquid films, Phys. Rev. Lett. 81 (1998) 3463, https://doi.org/10.1103/PhysRevLett.81.3463, https://journals.aps.org/prl/abstract/10.1103/PhysRevLett.81.3463.

[16] K. Kargupta, A. Sharma, Templating of thin films induced by dewetting on patterned surfaces, Phys. Rev. Lett. 86 (2001) 4536, https://doi.org/10.1103/PhysRevLett.86.4536, https://journals.aps.org/prl/abstract/10.1103/PhysRevLett.86.4536.

[17] E. Manev, R. Tsekov, B. Radoev, Effect of thickness non-homogeneity on the kinetic behaviour of microscopic foam film, J. Dispers. Sci. Technol. 18 (1997) 769–788, https://doi.org/10.1080/01932699708943771.

[18] R. Tsekov, The R4/5-problem in the drainage of dimpled thin liquid films, Colloids Surf. A, Physicochem. Eng. Asp. 141 (1998) 161–164, https://doi.org/10.1016/S0927-7757(97)00253-7.

[19] V. Chandran Suja, A. Kar, W. Cates, S.M. Remmert, G.G. Fuller, Foam stability in filtered lubricants containing antifoams, J. Colloid Interface Sci. 567 (2020) 1–9, https://doi.org/10.1016/j.jcis.2020.01.103.

[20] D.Y.C. Chan, E. Klaseboer, R. Manica, Film drainage and coalescence between deformable drops and bubbles, Soft Matter 7 (2011) 2235–2264, https://doi.org/10.1039/C0SM00812E.

[21] D.Y. Chan, E. Klaseboer, R. Manica, Theory of Non-equilibrium Force Measurements Involving Deformable Drops and Bubbles, 2011.

[22] J.M. Frostad, D. Tammaro, L. Santollani, S. Bochner de Araujo, G.G. Fuller, Dynamic fluid-film interferometry as a predictor of bulk foam properties, Soft Matter 12 (2016) 9266–9279, https://doi.org/10.1039/C6SM01361A.

[23] J.M. Frostad, J. Walter, L.G. Leal, A scaling relation for the capillary-pressure driven drainage of thin films, Phys. Fluids 25 (2013), https://doi.org/10.1063/1.4807069.

[24] L. Lombardi, D. Tammaro, P.L. Maffettone, Wimpled thin films via multiple motions of a bubble decorated with surface-active molecules, J. Colloid Interface Sci. 677 (2025) 521–528, https://doi.org/10.1016/J.JCIS.2024.07.208.

[25] L.Y. Clasohm, J.N. Connor, O.I. Vinogradova, R.G. Horn, The "wimple": rippled deformation of a fluid drop caused by hydrodynamic and surface forces during thin film drainage, Langmuir 21 (2005) 8243–8249, https://doi.org/10.1021/la0508588.

[26] Y. Wang, J. Frechette, Morphology of soft and rough contact via fluid drainage, Soft Matter 14 (2018) 7605–7614, https://doi.org/10.1039/C8SM00884A, https://pubs.rsc.org/en/content/articlehtml/2018/sm/c8sm00884a, https://pubs.rsc.org/en/content/articlelanding/2018/sm/c8sm00884a.

[27] V. Chandran Suja, M. Rodríguez-Hakim, J. Tajuelo, G.G. Fuller, Single bubble and drop techniques for characterizing foams and emulsions, https://doi.org/10.1016/j.cis.2020.102295, 2020.

[28] R.S. Allan, G.E. Charles, S.G. Mason, The approach of gas bubbles to a gas/liquid interface, J. Colloid Sci. 16 (1961) 150–165.
[29] N.S. Deshpande, M. Barigou, Foam flow phenomena in sudden expansions and contractions, Int. J. Multiph. Flow 27 (2001) 1463–1477, https://doi.org/10.1016/S0301-9322(01)00017-9.
[30] H.C. Pumphrev, L.A. Crum, Free oscillations of near-surface bubbles as a source of the underwater noise of rain, J. Acoust. Soc. Am. 87 (1990) 142–148, https://doi.org/10.1121/1.399306, /asa/jasa/article/87/1/142/680301/Free-oscillations-of-near-surface-bubbles-as-a.
[31] J.M. Brett, A. Krelle, A study of bubble collapse pressure pulse waves from small scale underwater explosions near the water surface, J. Sound Vib. 435 (2018) 91–103, https://doi.org/10.1016/J.JSV.2018.08.004.
[32] K.L. De Graaf, I. Penesis, P.A. Brandner, Modelling of seismic airgun bubble dynamics and pressure field using the Gilmore equation with additional damping factors, Ocean Eng. 76 (2014) 32–39, https://doi.org/10.1016/J.OCEANENG.2013.12.001.
[33] R. Suzuki, Y. Oda, D. Omata, N. Nishiie, R. Koshima, Y. Shiono, Y. Sawaguchi, J. Unga, T. Naoi, Y. Negishi, S. Kawakami, M. Hashida, K. Maruyama, Tumor growth suppression by the combination of nanobubbles and ultrasound, Cancer Sci. 107 (2016) 217–223, https://doi.org/10.1111/CAS.12867, https://onlinelibrary.wiley.com/doi/full/10.1111/cas.12867, https://onlinelibrary.wiley.com/doi/abs/10.1111/cas.12867, https://onlinelibrary.wiley.com/doi/10.1111/cas.12867.
[34] G. Lin, J.M. Frostad, G.G. Fuller, Influence of interfacial elasticity on liquid entrainment in thin foam films, Phys. Rev. Fluids 3 (2018) 114001, https://doi.org/10.1103/PhysRevFluids.3.114001.
[35] E. Chatzigiannakis, P. Veenstra, D. Ten Bosch, J. Vermant, Mimicking coalescence using a pressure-controlled dynamic thin film balance, Soft Matter 16 (2020) 9410–9422, https://doi.org/10.1039/D0SM00784F, https://pubs.rsc.org/en/content/articlehtml/2020/sm/d0sm00784f, https://pubs.rsc.org/en/content/articlelanding/2020/sm/d0sm00784f.
[36] S. Baas, V. Saggiomo, Ender3 3D printer kit transformed into open, programmable syringe pump set, HardwareX 10 (2021) e00219, https://doi.org/10.1016/j.ohx.2021.e00219.
[37] V. Chandran Suja, J.M. Frostad, G.G. Fuller, Impact of compressibility on the control of bubble-pressure tensiometers, Langmuir 32 (2016) 12031–12038, https://doi.org/10.1021/ACS.LANGMUIR.6B03258/ASSET/IMAGES/LARGE/LA-2016-03258C_0008.JPEG, https://pubs.acs.org/doi/full/10.1021/acs.langmuir.6b03258.
[38] D. Langevin, Surface shear rheology of monolayers at the surface of water, Adv. Colloid Interface Sci. 207 (2014) 121–130, https://doi.org/10.1016/J.CIS.2013.10.030.
[39] Z.A. Zell, A. Nowbahar, V. Mansard, L.G. Leal, S.S. Deshmukh, J.M. Mecca, C.J. Tucker, T.M. Squires, Surface shear inviscidity of soluble surfactants, Proc. Natl. Acad. Sci. USA 111 (2014) 3677–3682, https://doi.org/10.1073/PNAS.1315991111/SUPPL_FILE/SM02.WMV, https://www.pnas.org/doi/abs/10.1073/pnas.1315991111.
[40] M. Saad Bhamla, C. Chai, M.A. Àlvarez-Valenzuela, J. Tajuelo, G.G. Fuller, Interfacial mechanisms for stability of surfactant-laden films, PLoS ONE 12 (2017) e0175753, https://doi.org/10.1371/JOURNAL.PONE.0175753, https://journals.plos.org/plosone/article?id=10.1371/journal.pone.0175753.
[41] V. Sharma, A. Jaishankar, Y.C. Wang, G.H. McKinley, Rheology of globular proteins: apparent yield stress, high shear rate viscosity and interfacial viscoelasticity of bovine serum albumin solutions, Soft Matter 7 (2011) 5150–5160, https://doi.org/10.1039/C0SM01312A, https://pubs.rsc.org/en/content/articlehtml/2011/sm/c0sm01312a, https://pubs.rsc.org/en/content/articlelanding/2011/sm/c0sm01312a.
[42] L.G. Cascão Pereira, O. Théodoly, H.W. Blanch, C.J. Radke, Dilatational rheology of BSA conformers at the air/water interface, Langmuir 19 (2003) 2349–2356, https://doi.org/10.1021/LA020720E/ASSET/IMAGES/LARGE/LA020720EF00012.JPEG, https://pubs.acs.org/doi/full/10.1021/la020720e.
[43] M. Campana, S.L. Hosking, J.T. Petkov, I.M. Tucker, J.R. Webster, A. Zarbakhsh, J.R. Lu, Adsorption of bovine serum albumin (BSA) at the oil/water interface: a neutron reflection study, Langmuir 31 (2015) 5614–5622, https://doi.org/10.1021/ACS.LANGMUIR.5B00646/SUPPL_FILE/LA5B00646_SI_001.PDF, https://pubs.acs.org/doi/full/10.1021/acs.langmuir.5b00646.
[44] D. Tammaro, V. Chandran Suja, A. Kannan, L.D. Gala, E. Di Maio, G.G. Fuller, P.L. Maffettone, Flowering in bursting bubbles with viscoelastic interfaces, Proc. Natl. Acad. Sci. USA 118 (2021), https://doi.org/10.1073/pnas.2105058118.
[45] B. Jachimska, M. Wasilewska, Z. Adamczyk, Characterization of globular protein solutions by dynamic light scattering, electrophoretic mobility, and viscosity measurements, Langmuir 24 (2008) 6867–6872, https://doi.org/10.1021/LA800548P/ASSET/IMAGES/LA-2008-00548P_M008.GIF, https://pubs.acs.org/doi/full/10.1021/la800548p.
[46] S. Yadav, S.J. Shire, D.S. Kalonia, Viscosity analysis of high concentration bovine serum albumin aqueous solutions, Pharm. Res. 28 (2011) 1973–1983, https://doi.org/10.1007/S11095-011-0424-7/FIGURES/8, https://link.springer.com/article/10.1007/s11095-011-0424-7.
[47] L.M. Kushner, B.C. Du, J. Mes, I. Hoffman, A viscometric study of the micelles of sodium dodecyl sulfate in dilute solutions, J. Res. Natl. Bur. Stand. 49 (1952).
[48] T.P. Niraula, S.K. Shah, S.K. Chatterjee, A. Bhattarai, Effect of methanol on the surface tension and viscosity of sodiumdodecyl sulfate (SDS) in aqueous medium at 298.15–323.15 K, Karbala Int. J. Mod. Sci. 4 (2018) 26–34, https://doi.org/10.1016/J.KIJOMS.2017.10.004.
[49] F. Janssen, A.G. Wouters, E. Chatzigiannakis, J.A. Delcour, J. Vermant, Thin film drainage dynamics of wheat and rye dough liquors and oat batter liquor, Food Hydrocoll. 116 (2021) 106624, https://doi.org/10.1016/J.FOODHYD.2021.106624.
[50] R.H. Davis, J.A. Schonberg, J.M. Rallison, The lubrication force between two viscous drops, Phys. Fluids A, Fluid Dyn. 1 (1989) 77–81, https://doi.org/10.1063/1.857525.
[51] S. Poulain, L. Bourouiba, Biosurfactants change the thinning of contaminated bubbles at bacteria-laden water interfaces, Phys. Rev. Lett. 121 (2018), https://doi.org/10.1103/PhysRevLett.121.204502.
[52] V. Chandran Suja, A. Kar, W. Cates, S.M. Remmert, P.D. Savage, G.G. Fuller, Evaporation-induced foam stabilization in lubricating oils, Proc. Natl. Acad. Sci. USA 115 (2018) 7919–7924, https://doi.org/10.1073/pnas.1805645115.
[53] L.G. Cascão Pereira, C. Johansson, C.J. Radke, H.W. Blanch, Surface forces and drainage kinetics of protein-stabilized aqueous films, Langmuir 19 (2003) 7503–7513.
[54] J.J. Valle-Delgado, J.A. Molina-Bolívar, F. Galisteo-González, M.J. Gálvez-Ruiz, A. Feiler, M.W. Rutland, Interaction forces between BSA layers adsorbed on silica surfaces measured with an atomic force microscope, J. Phys. Chem. B 108 (2004) 5365–5371, https://doi.org/10.1021/jp0374197.
[55] L.G. Leal, Advanced Transport Phenomena: Fluid Mechanics and Convective Transport Processes, vol. 7, Cambridge University Press, 2007.
[56] E. Klaseboer, R. Manica, D.Y. Chan, Universal behavior of the initial stage of drop impact, Phys. Rev. Lett. 113 (2014) 194501, https://doi.org/10.1103/PHYSREVLETT.113.194501/FIGURES/4/MEDIUM, https://journals.aps.org/prl/abstract/10.1103/PhysRevLett.113.194501.
[57] R. Tsekov, E. Evstatieva, A fractal classification of the drainage dynamics in thin liquid films, Prog. Colloid & Polym. Sci. 126 (2004) 93–96, https://doi.org/10.1007/B93984/COVER, https://link.springer.com/chapter/10.1007/b93984.
[58] Z. Ren, Y. Guo, C.-H. Liu, P.-X. Gao, Hierarchically nanostructured materials for sustainable environmental applications, Front. Chem. 1 (2013), https://doi.org/10.3389/fchem.2013.00018.
[59] H. Sun, B. Marelli, Growing silk fibroin in advanced materials for food security, MRS Commun. 11 (2021) 31–45, https://doi.org/10.1557/s43579-020-00003-x.
[60] L. Lombardi, S. Consalvo, C. Esposito, D. Tammaro, Tailoring texture and functionality of vegetable protein meat analogues through 3D printed porous structures, Food Hydrocoll. 159 (2025) 110611, https://doi.org/10.1016/j.foodhyd.2024.110611.
[61] P.-c. Hu, D. Chang, J.-b. Tan, R.-t. Yang, H.-x. Yang, H.-j. Fu, Displacement measuring grating interferometer: a review, Front. Inf. Technol. Electron. Eng. 20 (2019) 631–654, https://doi.org/10.1631/FITEE.1800708.